Earth and Planetary Science Letters 604 (2023) 118006

Contents lists available at ScienceDirect

Earth and Planetary Science Letters

journal homepage: www.elsevier.com/locate/epsl

Weathering-driven porosity generation in altered oceanic peridotites

Simone Pujatti [a,*], Oliver Plümper [b], Benjamin M. Tutolo [a]

[a] Department of Geoscience, University of Calgary, Calgary, AB T2N 1N4, Canada
[b] Department of Earth Sciences, Utrecht University, Utrecht, 3584 CB, the Netherlands

ARTICLE INFO

Article history:
Received 15 September 2022
Received in revised form 22 December 2022
Accepted 9 January 2023
Available online 23 January 2023
Editor: A. Jacobson

Keywords:
seafloor weathering
olivine dissolution
dissolution channel
porosity generation
elemental flux

ABSTRACT

Ultramafic rocks exposed at slow and ultra-slow spreading mid-ocean ridges represent a significant and extremely reactive portion of the oceanic lithosphere. Thus, mechanistic understanding of the processes by which seawater infiltrates into and reacts with these rocks is essential for constraining their contribution to the chemistry of the oceans and the coupled carbonate-silicate cycle. Recent observations indicate that nanoscale processes contribute to seawater-driven alteration of ultramafic rocks, but conventional petrographic and tomographic observations of the associated physical features are challenging to link to these nanoscale features. Moreover, multiple generations and varying conditions of fluid infiltration often obscure the relative roles of higher-temperature serpentinization, where reactions are mostly isochemical, and lower-temperature weathering reactions, where observations suggest the release of massive amounts of magnesium. Here we bridge these scales and investigate the specific role of weathering processes in dissolution-driven porosity generation by integrating focused ion beam scanning electron microscopy nanotomography and micro-computed X-ray tomography imaging of the pore structures preserved in drill cores of serpentinized oceanic peridotites. Relict olivine crystals in all imaged samples contain abundant etch pits, and those in the higher-resolution FIB-SEM imagery show the presence of channel-like dissolution structures. The pore channels preferentially affect olivine along grain boundaries and show anisotropic distribution likely controlled by crystallographic features. The pores formed via olivine dissolution are interpreted to result from dissolution of serpentinized peridotite at conditions where serpentine and carbonate precipitation are kinetically inhibited, i.e., at weathering conditions. Importantly, the calculated connectivity of the imaged pore structures increases as the scale of investigation increases, suggesting that weathering-driven olivine dissolution facilitates further seawater infiltration and olivine dissolution, a positive feedback that can sustain continued magnesium extraction until the rocks are ultimately cut off from seawater circulation via sedimentation. Thus, while much attention has been directed towards constraining geochemical fluxes from the higher-temperature alteration of ultramafic rocks, our results support literature studies suggesting that mineral dissolution, and hence elemental fluxes, are significant at the lower temperatures of seafloor weathering. Our data thus provide mechanistic evidence of the physical process contributing to the observed elemental loss from weathered oceanic peridotites.

1. Intro

Decades of seafloor dredging and oceanic drilling have demonstrated that ultramafic rocks are frequently exposed at slow and ultra-slow spreading mid-ocean ridges (Warren, 2016). They constitute a significant portion of slow-spreading oceanic crust and make up an estimated 20-25% of the crust generated at slow-spreading ridges (Cannat et al., 2010). Ultramafic rocks equilibrate in the lithospheric mantle at high temperature at nominally anhydrous conditions and are, therefore, chemically unstable and thus highly reactive when exposed to near-surface, fluid-saturated conditions (Beinlich et al., 2018). Harzburgites, which are composed of olivine (forsterite-enriched) and orthopyroxene (enstatite-enriched), with minor amounts of clinopyroxene and spinel, represent 75% of the recovered peridotites sampled near the Mid-Atlantic Ridge (MAR), the most frequently sampled slow-spreading ridge environment (Warren, 2016).

Natural samples of oceanic peridotites are typically heavily altered and the primary textures and mineralogic associations are not preserved, except for spinel (Yu and Tikoff, 2020). Alteration results from the chemical and mineralogic changes that occur during the interaction between ultramafic rocks and seawater and/or

* Corresponding author.
E-mail address: pujatti.simone@ucalgary.ca (S. Pujatti).

https://doi.org/10.1016/j.epsl.2023.118006
0012-821X/

hydrothermal fluids. The former case is termed "seafloor weathering", which consists of (oxidative) alteration of the upper several hundreds of meters of seafloor-exposed ultramafic rocks and is often accompanied by the precipitation of secondary carbonate minerals (Bach et al., 2013; Kelemen et al., 2011). On the other end of the spectrum, the interaction between ultramafic lithologies and hydrothermal fluids includes a series of metasomatic reactions that occur at intermediate to high temperatures (up to ∼400 °C) and range from serpentinization to chloritization, epidotization, steatization, rodingization and listvenization (Bach et al., 2013).

The variability of alteration styles that affect ultramafic rocks in the oceanic lithosphere can make it challenging to identify the specific contribution of each reaction process, and the effects of high-temperature hydrothermal reactions can be difficult to separate from low-temperature weathering processes (Bach et al., 2011). Serpentinization is a hydration reaction and the most common type of hydrothermal alteration that affects ultramafic rocks. It is typically accompanied by minimal mobility of major elements, with serpentinization-derived fluids containing minimal concentrations of Mg and SiO_2 (Seyfried et al., 2015), the primary components of the mineral olivine and orthopyroxene of which the rocks are composed. Unfortunately, specific serpentinization reactions can be challenging to recognize, because a single specimen of peridotite can be subject to multiple fluid infiltration events, at varying temperature and pressure conditions, and ultimately be characterized by complex alteration patterns (e.g., Andréani et al., 2007). On the other hand, low-temperature seafloor weathering often overprints the initial, higher-temperature phase of water-driven alteration. It can be expressed in the form of olivine and brucite dissolution (Snow and Dick, 1995; Klein et al., 2020) and accompanying Mg release, or carbonate mineralization of relict olivine and/or serpentine/brucite (Bach et al., 2011), where Mg can also be mobilized (de Obeso et al., 2021). Thus, it can be extremely challenging to identify the specific alteration processes affecting an ultramafic rock sample and their relative contributions to elemental fluxes. Nevertheless, because of the relative abundance and exceptional reactivity of ultramafic rocks in oceanic settings, it is essential to mechanistically constrain these reaction processes to assess their role in controlling the chemical composition of the oceans and contributing to seafloor weathering feedbacks on the global carbon cycle (Brady and Gíslason, 1997; Coogan and Gillis, 2013; Krissansen-Totton and Catling, 2017).

Hydration associated with serpentinization reactions and carbonation associated with seafloor weathering require inputs of H_2O for the former and CO_2 for the latter, which in turn rely on the presence of pore space. Pores act as pathways that permit the infiltration of fluids and solutes through the rock system to reach pristine mineral surfaces and progress the reaction. Hydration of peridotite can be kinetically limited at low temperatures (Tutolo et al., 2018), whereas carbonation reactions are kinetically fast and typically transport-limited (Xiong and Giammar, 2014), thus their progress is dependent on the ability of fluids and solute to infiltrate into fresh portions of the rock (Kelemen and Hirth, 2012; Plümper et al., 2012; Tutolo et al., 2016). Therefore, the alteration of peridotite can be strongly affected by grain-scale microstructures, which controls the local hydrology and determine the spatial distribution of precipitate in the system (Lacinska et al., 2017). Electron microscopy and neutron scattering studies (Andréani et al., 2004; Boudier et al., 2010; Tutolo et al., 2016) have revealed the presence of nanometer-sized pores in altered peridotite, and the spatial distribution of pore structures at micrometric scale has been observed in both experimentally and naturally altered peridotite (Jöns et al., 2017; Osselin et al., 2022).

Here, we bridge observations from nm- to µm-scale to examine pore structures in serpentinized peridotites and constrain the nature of porosity generation and evolution during the alteration of peridotite. We observe an array of sizeable pores with smooth walls and channel-like morphologies, formed via the dissolution of brucite and/or olivine. The absence of secondary precipitates in these pores demands a mechanism for de-coupling dissolution of Mg-rich minerals from secondary phase precipitation, which is consistent with rapid olivine dissolution and kinetically inhibited Mg-silicate and Mg-carbonate precipitation at the low temperatures of seafloor weathering (below approximately 100 °C, Snow and Dick, 1995; Bach and Früh-Green, 2010). This mechanism opens connected fluid-pathways and increases the susceptibility of ultramafic rocks to seawater-driven chemical and heat extraction. In this way, our findings provide a specific, physical link between observed, multi-scale pore structures and their alteration processes. These findings further help to explain past observations of extensive Mg loss during weathering of oceanic peridotite.

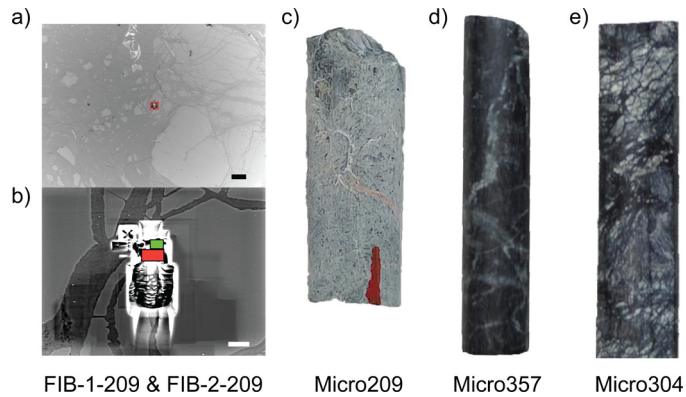

Fig. 1. Samples investigated in this study. a) BSE image showing the location of FIB-SEM cuttings: the FIB-SEM data sets were acquired from kernel-textured olivine. The large grains on the right side of the image are pyroxene crystals. Black scale bar = 200 µm. b) zoomed image showing the area marked by a red rectangle in Fig. 1a. The location of FIB-1-209 is marked by the green rectangle, the location of FIB-2-209 is marked by a red rectangle. White scale bar = 10 µm. c) Micro209 (mini)core with approximate diameter of 6 mm. The red marking at the base of the sample was made to ease the identification of its orientation. d) Micro357 (mini)core, with an approximate diameter of 5 mm. A white talc vein can be seen crossing the sample. e) Micro 304 (mini)core, with an approximate diameter of 5 mm. Remnants of pyroxene are light-colored and present throughout the sample.

2. Methods

2.1. Geological samples

The analyzed samples are shown in Fig. 1, and Table 1 reports the abbreviated names used throughout the text to refer to the samples, the analytical techniques employed, the resulting voxel dimensions, mineral modes, and serpentinization degree of the samples. The mineral assemblage and modes were estimated via visual inspection of thin section (FIB-1-209, FIB-2-209) and tomographic volumes (Micro209, Micro357, Micro304). A more detailed summary of the drilling sites described in this section can be found in the Supplementary Materials Section S.1, and a scan of the thin section from which FIB-1-209 and FIB-2-209 were collected is shown in Fig. S1.

2.1.1. Leg 209 data sets FIB-1-209 and FIB-2-209

Ocean Drilling Program (ODP) Leg 209 was carried out in 2003 and resulted in drilling at eight sites from 14°43′ to 15°44′N along the Mid-Atlantic Ridge, on well-exposed outcrops of peridotite found on both sides of the rift valley (Kelemen et al., 2004). Leg 209 investigated the processes that control the generation of oceanic lithosphere at magma-starved ridge sections. Site 1274 is the northernmost drill location along the rift valley and is found

Table 1
Sample names adopted in the main text, summary of analytical techniques employed with obtained voxel dimensions, serpentinization degrees and mineral assemblage.

IODP/ODP sample name	Renamed data set	Analysis technique	Voxel dimensions	Serpentinization degree (%)	Mineral assemblage[a]
ODP 209-1274-A-3R1 61-71	FIB-1-209	FIB-SEM	X, Y = 2 nm; Z = 10 nm	85%	Ol = 6%; prx (+ bastite) = 9%; spl = <1%; spr = 85%
ODP 209-1274-A-3R1 61-71	FIB-2-209	FIB-SEM	X, Y = 8 nm; Z = 10 nm		
ODP 209-1272-A-21R1 55-57	Micro209	μ-CT	X, Y, Z = 1.6 µm	99%	Ol = 1-2%; prx (bastite) = 10%; spl = <1%; srp = >95%
IODP 357-72-B-8R2 47-49	Micro357	μ-CT	X, Y, Z = 1.6 µm	65%	Ol = 7%; prx (+ bastite) = 7%; spl = 1%; tlc = 20%; srp = 65%
IODP 304-1309B-11R1 110-114	Micro304	μ-CT	X, Y, Z = 1.6 µm	75%	Ol = 4%; prx (+ bastite) = 20%; spl = <2%; srp = 75%

[a] Micro209 was almost entirely serpentinized, all the pyroxene was present as bastite recognized by pseudomorphic replacement of serpentine oriented along cleavage planes. Micro357 and Micro304 contained both unreplaced pyroxene and bastite, and the reported % values for Micro357 and Micro304 are a sum of remnant pyroxene plus bastite replacements. Ol = olivine remnants, prx = pyroxene, spl = spinel, tlc = talc, srp = serpentine.

∼31 km north of the western intersection between MAR and the 15°20′ Fracture Zone, recovering mainly peridotites and few meter-scale gabbroic intrusions (Kelemen et al., 2004). Seafloor weathering alteration at Site 1274 is recognized in the uppermost ∼90 m of hole penetration in the form of oxidative carbonates and iron oxyhydroxides-clay alteration veins and haloes. Core Section 209-1274-A-3R1 is made chiefly of harzburgite with subordinate dunite bands that have been heavily serpentinized. Sample 209-1274-A-3R1 61-71 was recovered from a representative portion of the overall core section at ∼17.51 meters below seafloor (mbsf) and is delimited at its top and bottom by the presence of orange iron oxyhydroxide and carbonate veins (Kelemen et al., 2004).

2.1.2. Leg 209 sample Micro209

Site 1272 was also drilled during ODP Leg 209 and is located on the western flank of the Mid-Atlantic rift valley, close to the top of the inside corner high, south of the 15°20′ Fracture Zone. The predominant alteration style identified at Hole 1272A is serpentinization. However, low-temperature oxidative alteration is also present in the form of red-brown clays and iron oxyhydroxides associated with aragonite veins and iowaite mineralization (Bach et al., 2004; Supplementary Material Section S.1.2). Several faults have been identified at Hole 1272A and their location is signaled by the presence of fault gouge and locally increased veining. Fault gouge is expected to be saturated with fluids and highly conductive to fluid flow compared to the surrounding wallrock (Kelemen et al., 2004). Sample Micro209 was recovered from a depth of ∼99.5 mbsf and is made of heavily serpentinized protogranular harzburgite. Pyroxene is only preserved as replacive bastite, as the sample is almost entirely serpentinized, with a low presence of olivine remnants (<2%, Table 1). Several interpreted faults have been identified in the vicinity of Micro209: at 89.7 mbsf in Section 19R-1; at 99.58 mbsf in Section 21R-1; at 100.6 mbsf in Section 21R-2; at 108.6 mbsf in Section 23R-1.

2.1.3. Expedition 357 sample Micro357

International Ocean Discovery Program (IODP) Expedition 357 drilled an east-west transect across the southern wall of the Atlantis Massif, an oceanic core complex (OCC) located ∼15 km west of the median-axis valley of the MAR, to investigate potential links between serpentinization processes and their influence on microbial populations in the shallow subseafloor. The sample analyzed here was recovered from Hole B at Site 72, located close to the summit of the corrugated detachment surface found on the top of the Atlantis Massif, to the north of the carbonate cap above the Lost City hydrothermal field. Hole B drilled through a section interpreted as a detachment fault zone located in serpentinized peridotite (Früh-Green et al., 2017). Sample Micro357 was recovered from ∼12 mbsf from an interval of serpentinized harzburgite that shows the presence of metasomatic talc-chlorite veins and patches. Sample Micro357 contains abundant talc and shows the lowest serpentinization degree reported in this study, with the highest preservation of olivine remnants. Within the same core section as sample Micro357, shipboard X-ray powder diffraction analyses identified the presence of carbonate in veins, which amounted to ∼6 wt%. Furthermore, photomicrographs collected during Expedition 357 from Micro357 show the presence of olivine neoblasts pseudomorphically replaced by carbonate minerals (Früh-Green et al., 2017).

2.1.4. Expedition 304/305 sample Micro304

IODP Expedition 304/305 targeted the Atlantis Massif at 30°N, to study the processes that determine the formation of oceanic core complexes and the exhumation of ultramafic lithologies to the seafloor. Site 1309 is situated on the central dome of the Atlantic Massif, where the latest and lowest-temperature metamorphic alteration is recorded by white veins infilled by carbonate and sulfide ± chlorite or carbonate associated with saponite. This stage is inferred to occur at low temperature, possibly at 100-120 °C, as recorded at the bottom of Hole 1309D (Blackman et al., 2006).

The sample analyzed in this study was recovered from serpentinized harzburgite recovered from Hole 1309B. Serpentine veins at this hole are commonly associated with fine-grained carbonate, which was also observed replacing ribbon-textured serpentine during IODP Expedition 304/305 (Blackman et al., 2006). Moreover, calcite and/or aragonite veins were locally recognized. The Micro304 sample was recovered from 58.1 mbsf and is part of an ultramafic unit made of protogranular harzburgite that records the contact with the upper gabbroic units. A mm-wide white zone of talc-tremolite-carbonate alteration is present at the contact between mafic and ultramafic rocks and intrudes into the ultramafic unit along fractures. Micro304 records an intermediate serpentinization degree and contained abundant pyroxene, both as bastite and unreplaced crystals.

2.1.5. Site variability

The samples included in this study were all recovered from the first 100 mbsf at drilling sites located at slow-spreading segments of the Mid-Atlantic Ridge and having young ages (<2 m.y., Grimes et al., 2008; Cooperdock and Stockli, 2018). All sites show evidence for low-temperature water-rock interactions in the form of

secondary mineral precipitates - carbonate and iron oxyhydroxides are the most common occurrences, together with iowaite identified during ODP Leg 209 and saponite recognized during IODP Expedition 304. All sites drilled through shallow and faulted sections of exposed oceanic lithosphere, where the faults could have acted as preferential pathways that facilitated the entrainment of seawater. All samples consist of serpentinized harzburgite, which was the dominant lithology retrieved from most drilling sites with the exception of IODP Expedition 304, which chiefly recovered gabbroic rocks. Micro357 presents some compositional variability as it was affected by silica metasomatism that overprinted serpentinization, producing thick talc veins.

2.2. Focused ion beam-scanning electron microscopy

Focused ion beam scanning electron microscopy (FIB-SEM) analyses were carried out on one thin section sourced from Ocean Drilling Program (ODP) core sample 209-1274-A-3R1 61-71. The data sets were collected with a FEI Helios NanoLab™ G3 DualBeam FIB-SEM at the Electron Microscopy Center at Utrecht University (NL) in backscattered mode and under a high vacuum. Regions of interest were identified at the contact between the serpentine matrix and unreplaced olivine crystals and coated with platinum to prevent beam damage during acquisition. The voxel dimensions in data set FIB-2-209 are 8 nm in the x and y directions and 10 nm along z. To characterize the presence of pores smaller than the voxel size of FIB-2-209, we collected data set FIB-1-209 next to the FIB-2-209 area. FIB-1-209 has voxel dimensions of 2 nm along x and y and 10 nm along z.

2.3. Synchrotron-based microtomography

Samples Micro209, Micro304, and Micro357 were prepared by grinding on a polishing wheel to obtain cylindric cores with an approximate diameter of 5 mm (∼6 mm for Micro209). The samples were scanned with a parallel, monochromatic X-ray beam on the Biomedical Imaging beamline of the Canadian Light Source (BMIT-ID, Wysokinski et al., 2015). The photon energy employed was 35-45 keV and varied depending on the sample thickness to achieve optimal transmission of ∼30%. Cubic voxels with dimensions of 1.6 µm were recorded with a PCO Edge 5.5 camera coupled to a 50 µm LuAG:Ce scintillator (Crytur) via an optical system (Optique Peter) with 4x magnification. The distance between the sample and detector was 20 cm and phase retrieval methods (Paganin et al., 2002) were applied to optimize the spatial coherence of the beam. The dynamic camera range was used at approximately 20% and 2000 projections were acquired. Data reconstruction was performed in tofu/ez-ufo software package (Faragó et al., 2022).

2.4. Processing, segmentation and quantification of tomographic data

All image processing and quantification of segmented pores were performed with the ThermoFisher Scientific PerGeos software package, whereas the segmentation steps were carried out with Object Research System (ORS) (Montreal, Quebec Canada) Dragonfly software. The micro-computed X-ray tomography (μ-CT) data sets required filtering of the raw data to obtain cleaner segmentation of the pore network. The same processing recipe has been employed for every sample to ensure consistency across the various data sets. The processing routine involved the initial application of a non-local means filter to remove image noise from the raw data and subsequent application of Sobel, Bilateral and Median filters. Finally, the resultant data sets were combined using the following equation:

$$I_{final} = \frac{Bilateral * Sobel}{256} + Median * \left(1 - \frac{Sobel}{256}\right) \quad (1)$$

Where I_{final} stands for final imaging result. When equation (1) is applied to 8-bit image data, it results in a grayscale image where voxels located at the edges of objects are identified by the Sobel filter and processed by Bilateral smoothing. Voxels that are not located on the edges of objects are instead smoothed according to the Median filter. The final step of the processing routine involved adjustment of the contrast and brightness of the data sets to facilitate the discrimination between dark areas indicative of pores and gray areas indicative of serpentine minerals. The segmentation of the porous regions was performed using an artificial intelligence algorithm with U-net architecture available in Dragonfly. Details about the training material employed for machine learning can be found in the Supplementary Material Section S.2.1.

The presence of intense shading and frequent ring artifacts precluded the quantification of the porosity content across the entire tomographic volume in sample Micro209. Therefore, local sub-volumes devoid of significant artifacts and showing relevant features were segmented individually. Hence, no statistically significant pore size distribution (PSD) could be extracted from sample Micro209. In samples Micro357 and Micro304, it was possible to segment and quantify the pore volume across the entire 3D volume, thus permitting a statistically significant determination of the PSD. The PSD was calculated by quantifying the volume of interconnected pores and assuming that the pore volume equates to a sphere whose diameter is the equivalent spherical diameter. To account for segmentation artifacts related to random noise in the background images, pores that contained less than nine voxels were excluded from computations in each data set. To interpret the distribution of the pore networks, pores with volumes smaller than 125 voxels have been removed from the visualizations. The Euler characteristic χ was calculated for each pore after an automatic separation step in PerGeos. The Euler characteristic is an indicator of the degree of connectivity of a structure, and negative values of χ indicate a higher degree of connectivity (Vogel et al., 2010). Further details about the calculation of χ values can be found in the Supplementary Material Section S.2.2.

3. Results

The textural distribution of analyzed pores and mineral phases for each sample shows characteristics typical of altered peridotites. FIB-SEM images and grain-scale observations demonstrate the incipient generation and growth of the pore network in the form of dissolution channels that affect olivine remnants (Fig. 2). At the micron-scale, μ-CT data illustrate that pores form clusters with a spatial distribution that is controlled by the presence of olivine remnants (Fig. 3). A summary of the abbreviated names used to refer to the analyzed samples and references to their full names can be found in Table 1.

3.1. FIB-1-209

FIB-SEM analyses of FIB-1-209 (Fig. 2a) represent the highest resolution imagery presented here and thus record the distribution of the finest pore sizes. In this data set, a broad crystal and isolated, smaller (∼1 µm along its longest dimension) grains of olivine are surrounded by a darker gray serpentine matrix. Two distinct size classes of pores are present: 1) nanometer-sized pores (with diameter < 30 nm), which are scattered through the serpentine matrix (visible as isolated dark dots); 2) coarser pores (diameter > ∼30 nm), which are located either at the grain boundary of the central olivine grain or within the unreplaced crystal, close to the grain boundary. The 3D reconstruction of FIB-1-209 (Fig. 4a)

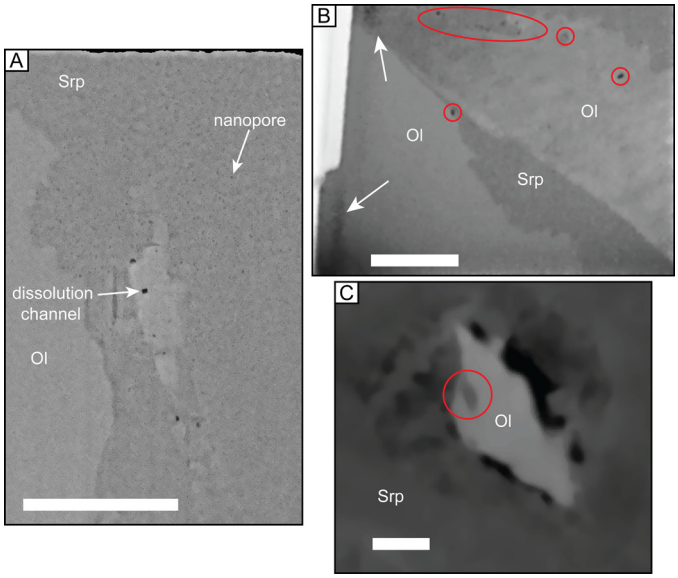

Fig. 2. Orthoslices presenting the results of FIB-SEM analyses and grain-scale observations. (a) FIB-SEM image, data set FIB-1-209. Nanometric pores are recognized in the serpentine matrix as small dark spots. Coarser dark spots found in contact with olivine are dissolution channels. Scale bar = 1 µm. (b) FIB-SEM image, data set FIB-2-209. White arrows point to shading artifacts that were excluded from the quantification of porosity. Red circles highlight the presence of pores. Scale bar = 1 µm. (c) μ-CT image, sample Micro209. Pores partially rim the grain boundary of olivine. An etch pit is highlighted with a red circle. Scale bar = 50 µm. Ol = olivine; Srp = serpentine.

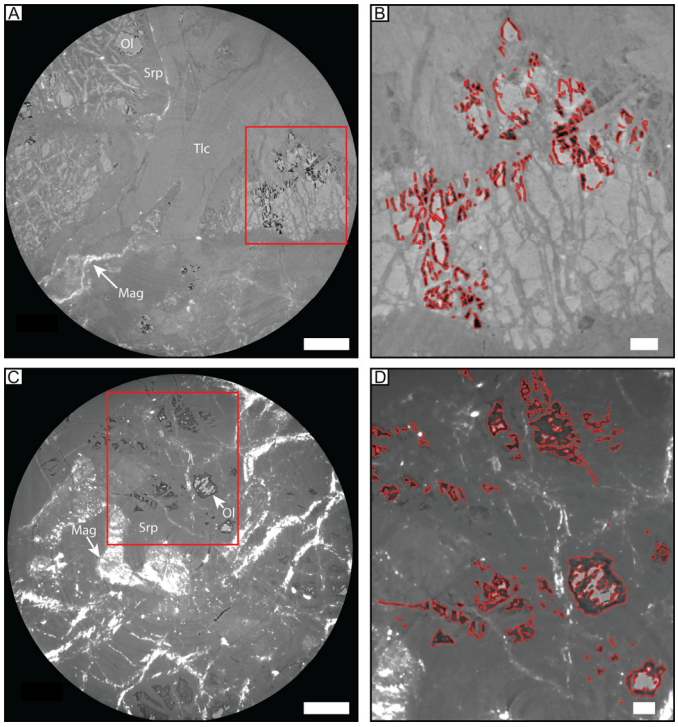

Fig. 3. Orthoslices depicting the results of core-scale observations from μ-CT data sets. (a) Sample Micro357, showing an association of olivine, serpentine, talc and magnetite. The red rectangle highlights an area rich in pores. Scale bar = 500 µm. (b) Close-up of the area outlined with a red rectangle in Fig. 2a. Pores outlined with red markings partly envelop olivine grains. Scale bar = 100 µm. (c) Sample Micro304. Bright magnetite in veins and pseudomorphic bastite (center-left of the image) in a serpentine matrix with sparse olivine crystals. (d) Close-up of the area highlighted with a red rectangle in Fig. 2c. The pores have been outlined with red markings. Scale bar = 100 µm. Ol = olivine; Mag = magnetite; Srp = serpentine; Tlc = talc.

shows that both classes of pores form channels that are subparallel and elongated along the *z*-direction of the tomographic volume. The coarse channels have dimensions < 200 nm (Fig. 5a) and have relatively smooth surfaces and conical shapes (e.g., Fig. 4a, top). They do not exhibit branching or significant lateral connectivity, as is confirmed by the observation that all calculated values of the Euler characteristic, χ, for this sample are $\geq$ -2 (Fig. 6a), which represents the least negative χ distribution (i.e., least connected) we report (Fig. 6).

3.2. FIB-2-209

FIB-SEM analyses of sample FIB-2-209 permitted to record pore structure with minimum sizes of 8 nm along the *x* and *y* directions and 10 nm along the *z* direction, thus having similar, but slightly coarser size than those of FIB-1-209 (Table 1). Similar to FIB-1-209, FIB-2-209 contains domains of olivine surrounded by a darker gray serpentine matrix. However, due to the lower resolution of data set FIB-2-209 compared to FIB-1-209 it is possible that the nanometer-sized pores were present also in data set FIB-2-209 but were less completely imaged (Fig. 2). Therefore, the population of pores identified from data set FIB-2-209 broadly corresponds to the coarser porosity observed in data set FIB-1-209. Pores in FIB-2-209 primarily occur at the grain boundary of unreplaced olivine grains (red circles in Fig. 2b). 3D visualization of the FIB-2-209 tomographic volume shows the presence of vertically elongated, channel-shaped pores that stretch along the grain boundaries of unreplaced olivine (e.g., Fig. 4b, top). The individual and separated pore channels initially observed in sample FIB-1-209 appear more evolved in FIB-2-209, with an increased degree of lateral connectivity indicative of pore coalescence as they evolve from linear towards more planar features. The increased degree of connectivity is reflected by more negative values of χ, down to -5, indicating that the coarser pore structures in FIB-2-209 are more than twice as connected as in FIB-1-209 (Figs. 6a and 6b). Overall, data sets FIB-1-209 and FIB-2-209 show comparable pore size distributions and connectivity values, with the difference that FIB-1-209 also captured isolated and nanometer-sized pores present in the serpentine matrix, which could not be detected in FIB-2-209 due to its lower spatial resolution.

3.3. Micro209

Processed sub-volumes from sample Micro209 contain olivine surrounded by serpentine, with porous areas located along the olivine-serpentine grain boundaries (Fig. 2c), similar to the texture identified in the previous two samples. However, in sample Micro209, the observed pores exist at a significantly larger (micrometric) scale, and their structure has evolved towards more planar morphologies – i.e., individual pores do not have circular outlines but develop laterally along the olivine-serpentine grain boundaries. Additionally, etch pits can be observed impinging into unreplaced olivine (e.g., Fig. 2c, red circle). In 3D, the pore structure envelopes the relict olivine, in direct contrast to the channeled pores observed at smaller scales in FIB-1-209 and FIB-2-209 (Figs. 2a and 2b, respectively). The lateral expansion appears to occur via the development of individual porosity channels that expand radially from the central pore mass. Fig. 6c shows that the most negative value of χ = -8 indicates that pores in sample Micro209 are marginally more connected than those in FIB-2-209 (χ = -5).

3.4. Micro357

The altered peridotite imaged in sample Micro357 is characterized by a central, conspicuous serpentine vein overprinted in its

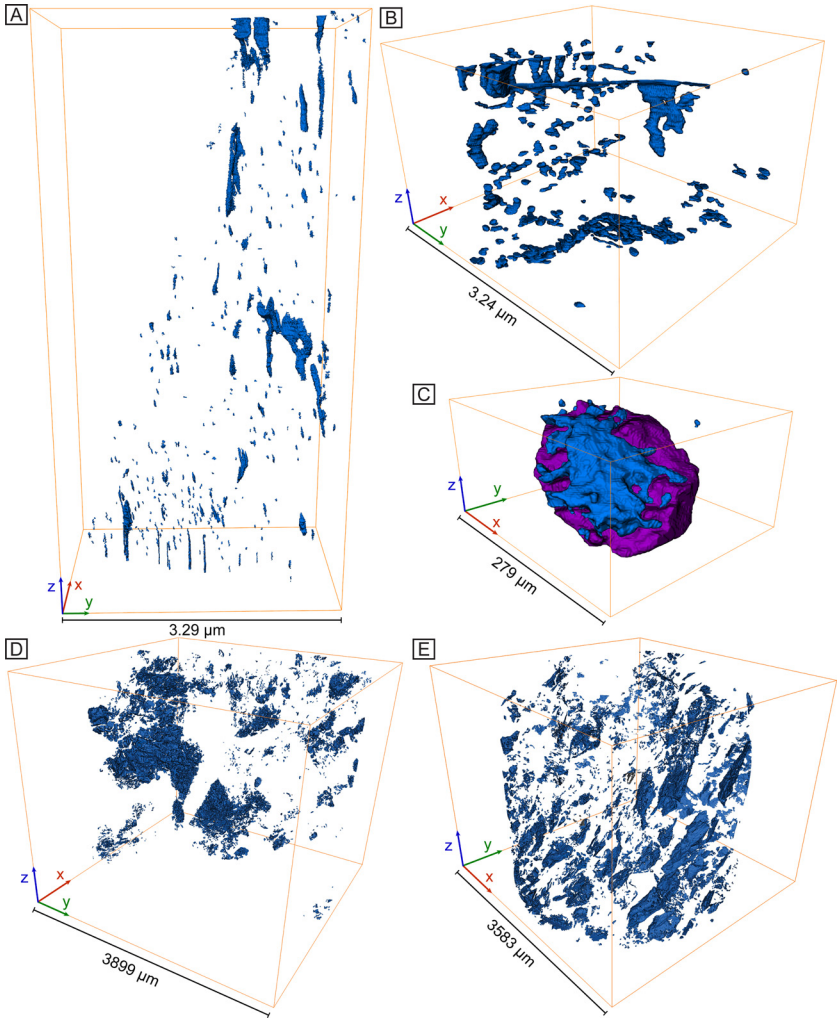

Fig. 4. Tomographic volumes reconstructed from FIB-SEM and μ-CT data sets. Pores smaller than 125 voxels have been hidden to ease the visualization of the main pore structures. (a) Data set FIB-1-209. Dimensions: x = 1.91 µm, y = 3.29 µm, z = 6.66 µm. (b) Data set FIB-2-209. Dimensions: x = 2.98 µm, y = 3.24 µm, z = 2.09 µm. (c) Sample Micro209, μ-CT data set. Purple = olivine; blue = pores. Dimensions: x = 279 µm, y = 256 µm, z = 139 µm. (d) Sample Micro357. Dimensions: x = 3899 µm, y = 3899 µm, z = 3454 µm. (e) Sample Micro304. Dimensions: x = 3583 µm, y = 3583 µm, z = 3023 µm.

center by talc. The other primary textural domain is made of remnants of olivine that range in size from ∼20 µm to ∼200 µm. They have been partly to fully replaced by serpentine and magnetite, forming a mesh texture (Fig. 3a, left side) where thin magnetite veinlets are aligned along the mesh rims. Olivine is also present in clusters devoid of oxides and dissected by serpentine veinlets (Fig. 3a, red rectangle). Similar to sample Micro209, pores are localized at olivine grain boundaries in both textures present in Micro357, and ∼6 µm to ∼20 µm thick pore structures envelop olivine remnants. The pores are best developed within the dissected olivine structure (e.g., Fig. 3a, red rectangle).

Nevertheless, not every olivine remnant is surrounded by pores, likely due to the distribution of local fluid pathways. 3D visualization demonstrates that the pores are organized in clusters - the central vein separates the two major pore clusters in Micro357 (Fig. 4d) imaged in this sample (Fig. 3a). The channel-shaped pores observed in the FIB-SEM data sets (Figs. 4a and 4b) cannot be identified in Micro357; at the scale of μ-CT analyses only coarser and more developed pore structure can be detected, which are recognized around unreplaced olivine remnants and more frequently encountered within the domains of dissected olivine. The PSD suggests coalescence of pores coinciding with the creation of a coarser pore network (Fig. 5c). Within this coarser pore network, more lateral connections between individual pores have formed, achieving higher calculated connectivity than all the samples described thus far (FIB-1-209, FIB-2-209, and Micro209). The two coarser connected pore volumes identified for Micro357 have χ of -491 and -847 (Fig. 6d), indicating a degree of connectivity that is two orders of magnitude greater than the previous samples.

3.5. Micro304

In sample Micro304, bright oxide minerals and scattered olivine grains are surrounded by a serpentine matrix that dominates the sample volumetrically (Fig. 3c). The oxides are organized in veins and secondary veinlets (Fig. 3c bottom left and top right) or in clusters associated with serpentine that pseudomorphically replace pyroxene (i.e., bastite, Fig. 3c center and top left). Olivine is present as isolated grains (Fig. 3c red rectangle) or small clusters made of several grains (Fig. 3c bottom). Olivine remnants show irregular morphologies that result from the presence of pores along its grain boundaries. In Micro304 porosity affects the rock so extensively that some grains of olivine have been completely removed, leaving behind voids that mimic the morphology of olivine fragments (Fig. 3d). Moreover, elongated etch pits can be seen protruding within domains of remnant olivine (Fig. 3d). Pores rimming olivine and etch pits observed in Micro304 are the most developed com-

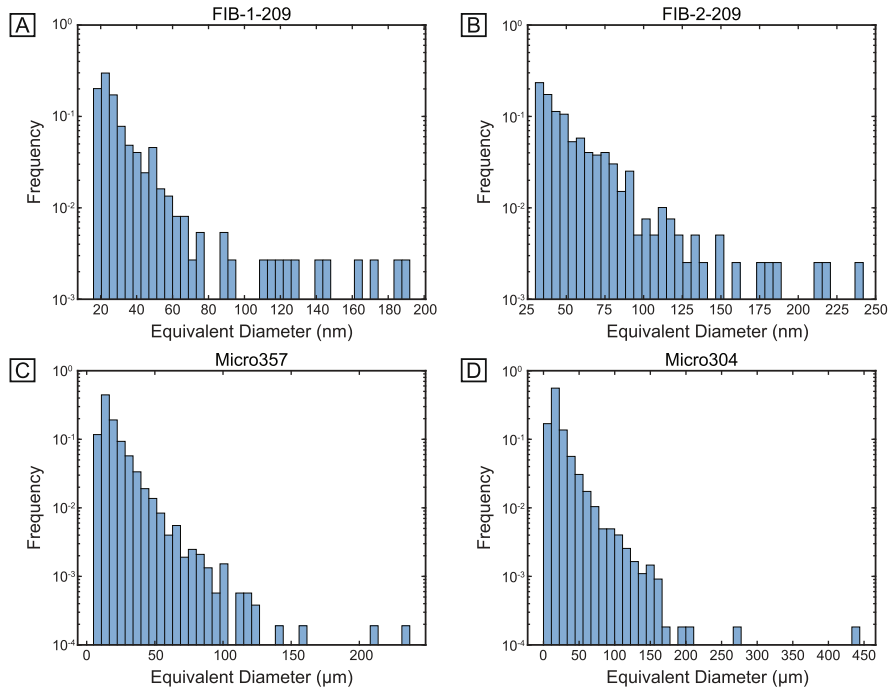

Fig. 5. Pore size distribution (PSD) of statistically significant quantifications of pore size distributions. Number of bins = 40. (a) PSD of sample 209-1274-A-3R1 61-71 data set FIB-1-209, n = 398. (b) PSD of sample 209-1274-A-3R1 61-71, data set FIB-2-209, n = 397. (c) PSD of sample Micro357, n = 5253. (d) PSD of sample Micro304, n = 5474.

pared to all studied samples, with pore size ranging from ∼6 μm to ∼50 μm.

The 3D pore network in Micro304 shows the presence of several coarse pore clusters that are preferentially oriented and slightly inclined compared to the vertical direction of the tomographic volume (Fig. 4e). Because the porosity is well developed, it affects the coarser grains of olivine. As a result, it forms large pore clusters more frequently than in Micro357, in which pores were primarily found around fine-grained olivine remnants. This aspect is reflected in the pore size distribution of Micro304, which shows both the presence of 2 large pores with sizes greater than 250 μm, and a higher abundance of pores ranging from 50 μm to 200 μm than Micro357 (Fig. 5d). However, the overall textural style in Micro357 and Micro304 appears similar, with pores located at the grain boundaries of olivine and enveloping its remnants. The preservation of the morphology inherited by olivine fragments can also be recognized in 3D, where the larger pores preserve prismatic shapes (Fig. 4e, most easily identified at the bottom-right side). Lateral coalescence of the pores in Micro304 is the most developed of all samples analyzed, and results in pores forming an almost continuous envelope around olivine crystals. This textural style leads to the formation of large pores, with the size of the individual pores depending on the grain size of primary olivine crystals, achieving in Micro304 a maximum equivalent diameter of ∼440 μm (Fig. 5d). Coarser pore sizes are accompanied by an enhanced degree of connectivity, evidenced by the recorded minimum χ value of -2785 (Fig. 6e).

4. Discussion

In this section, we describe the preferential orientation of pores observed in our FIB-SEM data sets and in Micro304 (Section 4.1), examine the potential of serpentinization processes to explain the genesis of the pore structures identified in the analyzed samples (Section 4.2), consider the spatial association of the samples to alteration features identified in the core sections from which the samples were sourced, and interpret the pore structures in a kinetic framework (Section 4.3). Finally, we explore the implications of our findings for interpreting the role of low-temperature peridotite weathering in ocean geochemistry and the coupled silicate-carbonate cycle (Section 4.4).

4.1. Anisotropic distribution of pores

Most segmented pores in the FIB-SEM data sets (Fig. 4a and 4b) are subparallel and display a preferential orientation, particularly evident in the dissolution channels. Several studies describing the anisotropic dissolution of olivine crystals have shown that the dissolution rate of olivine is fastest along its crystallographic b-axis (Grandstaff, 1978; Awad et al., 2000; King et al., 2014; Peuble et al., 2015). Anisotropic dissolution has been suggested to arise from the preferential orientation of M(1) crystallographic sites in olivine parallel to [010]. M(1)-oxygen bonds attain a more negative charge than M(2)-oxygen bonds, leading to more favorable protonation of oxygen bond to the M(1) sites (Awad et al., 2000). Alternatively, the elongated shape of the pore channels could result from preferential dissolution along olivine subgrain walls; however, their presence could not be assessed with the analytical approach employed in this study. At the micrometer-scale, preferential orientation of the coarser pores was recognized in Micro304 (Fig. 4e). Because the pores in Micro304 form envelopes around olivine grains, the observed preferential pore orientation may result from the anisotropic distribution of primary olivine crystals. Crystallographic preferred orientations (CPOs) similar to the preferential orientations recognized in this study have been identified elsewhere and attributed to the action of the asthenospheric mantle flow, that via plastic deformation leads to subgrain wall formation with statistically non-random distribution and consequent alignment of subgrain walls creating a CPO, with the (010) planes orienting subparallel to the direction of the mantle flow (Peuble et al., 2015). The pores observed in this study are located at the grain boundaries of olivine, consequently the preferential orientation of the olivine grains is likely to control the spatial distribution of the pores.

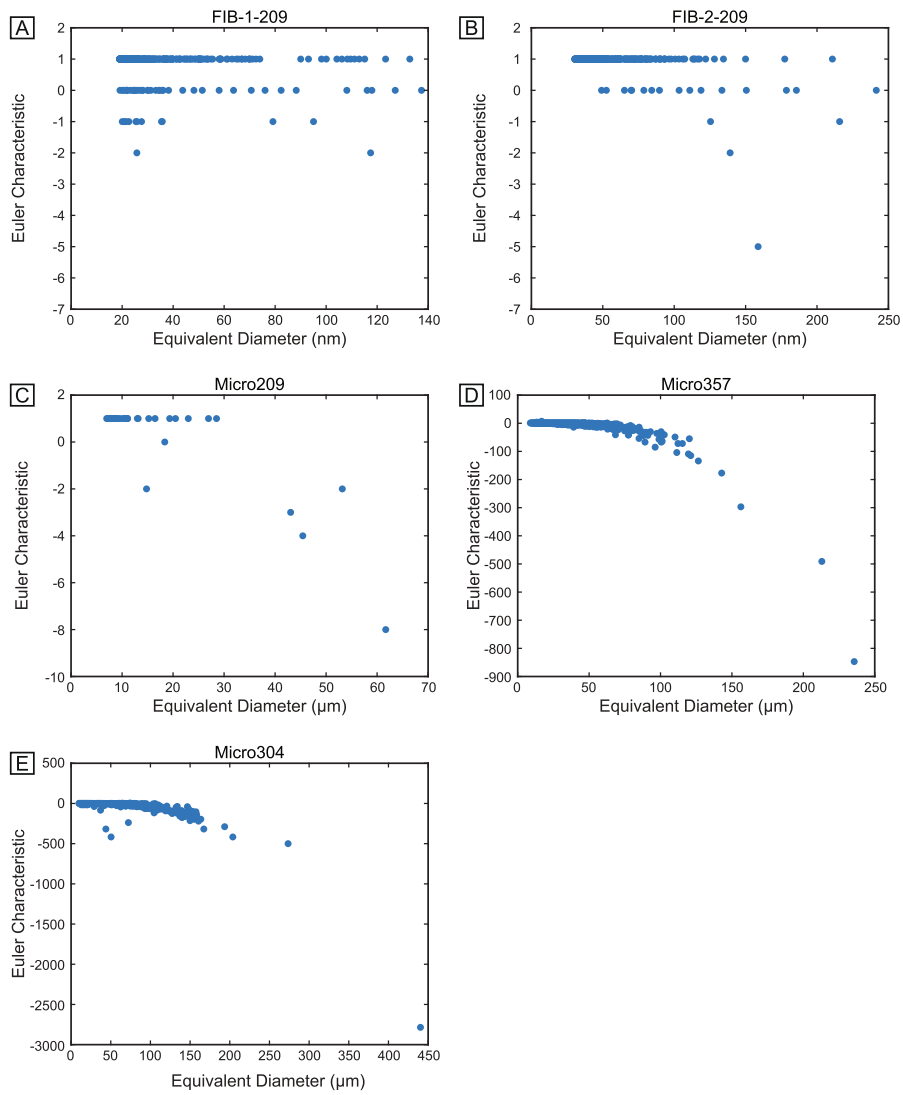

Fig. 6. Plots of Euler characteristic values as a function of the equivalent spheric diameter. More negative values of the Euler characteristic (χ) represent increased degree of connectivity. (a) Sample 209-1274-A-3R1 61-71 data set FIB-1-209, n = 398. Minimum χ = -2. (b) Sample 209-1274-A-3R1 61-71, data set FIB-2-209, n = 397. Minimum χ = -5. (c) Sample Micro209, n = 36. Minimum χ = -8. (d) Sample Micro357, n = 5253. Minimum χ = -847. (e) Sample Micro304, n = 5474. Minimum χ = -2785.

4.2. Serpentinization-generated nanopores

Serpentinization is the main style of hydrothermal alteration in samples investigated here, and also the most commonly identified alteration style in peridotite cores drilled from the oceanic crust, thus we explore its potential to explain the observed pore textures. Notably, all of our tomographic data sets are characterized by an absence of secondary phases filling the pores located at olivine grain boundaries. Thus, any geochemical process capable of explaining the textures reported here must be consistent with the lack of in situ precipitation of secondary products.

Serpentinization reactions are commonly understood in terms of an interface-coupled dissolution-precipitation mechanism (ICDP, Plümper et al., 2012), which involves the formation of secondary phases in a thin fluid film located at the interface with reacting primary minerals. Local precipitation of alteration phases is central to the ICDP mechanism, because it leads to the local buildup of differential stresses due to the increase in solid volume when primary phases are converted to secondary minerals, ultimately leading to fracturing of the rock that generates new pores. However, because the pore morphologies we observe (Fig. 4) are not planar, they could not have formed due to fracturing. Nevertheless, neutron scattering studies (Tutolo et al., 2016) suggest that the formation of new pores accompanies serpentinization reactions. The newly generated pores are expected to be nanometer-sized (Tutolo et al., 2016), and thus likely correspond to the nanopores identified within the serpentine matrix only in our highest-resolution data set FIB-1-209 (Fig. 2a). These pores were noticed only in the serpentine matrix and are not associated with other mineral phases. Moreover, due to the low reactivity of serpentine in seawater-derived fluids at low temperatures (Luce et al., 1972; Bales and Morgan, 1985), we conclude that this specific, nanometer-sized grouping of pores formed during serpentinization reactions. The pore structure shown by natural and experimentally serpentinized olivine crystals typically consists of funnel-shaped etch pits that evolve to networks of polyhedral and pyramidal mounts that impart an indented morphology to the altered olivine grains, and generally are distributed homogeneously across crystal faces (Lafay et al., 2012). The pore structures that affect olivine grains observed in our FIB-SEM data sets are strikingly different, showing sparse pores with high aspect ratio that penetrate deeply into olivine fragments, forming elongated dissolution channels. Due to the lack of textural similarities between the planar fractures or funnel-shaped etch pits expected to form due to serpentiniza-

tion reactions (Plümper et al., 2012) and the elongated dissolution channels shown in this study, we conclude that the pores associated with olivine dissolution formed by some process other than serpentinization (Velbel, 2009).

4.3. Porosity generation during seafloor weathering

The samples analyzed here were all recovered from drilling sites that showed extensive evidence of seawater-driven low-temperature alteration (e.g., carbonate veins, oxidative haloes, and, in Leg 209 rocks, iowaite and nontronite mineralization, Supplementary Material Section S.1). Most samples were in close proximity to carbonate precipitates (Section 2.1, Supplementary Material Section S.1), suggestive of seawater infiltration (Bach et al., 2011) except for Micro209, which was close to several interpreted faults that likely acted as pathways for focused fluid flow in the subseafloor (Bach et al., 2004; Section 2.1.2; Supplementary Material Section S.1.2). Open-system conditions consistent with these observations would result in open pore space that lacks in situ precipitate by preventing attainment of the extreme levels of supersaturation required to precipitate secondary Mg-silicates (Arizaleta et al., 2020; Che et al., 2021; Mulders and Oelkers, 2021; Tosca, 2015) and carbonates (Berninger et al., 2014; Power et al., 2017) at low temperatures (i.e., < 100 °C, Snow and Dick, 1995; Bach and Früh-Green, 2010) by exporting Mg and Si in reaction fluids, away from the reaction interface. Because olivine dissolution is very rapid at the aforementioned conditions (log rate = ∼-10 mol/m^2/s at pH = 8 and T = 25 °C, Oelkers et al., 2018), secondary phase precipitation becomes the rate-limiting step (Tutolo et al., 2018) and net Mg and Si export in the fluid phase can thus be achieved. In this scenario, secondary minerals will be precipitated at a hydrologically-controlled distance from the location of olivine dissolution (e.g., stagnation points where fluids experience longer residence time), if at all. Recent experiments examining olivine dissolution in seawater at ambient temperatures support this observation – although $CaCO_3$ can readily precipitate during early stages of seawater-olivine interaction, Mg-carbonates do not, and Mg-silicates precipitate sluggishly (Fuhr et al., 2022). Together, these observations suggest that the pore textures examined here formed due to the interaction between seawater and harzburgites at temperatures close to ambient conditions (< 100 °C, Snow and Dick, 1995; Bach and Früh-Green, 2010), a process commonly referred to as seafloor weathering. Open-system conditions required by seafloor weathering reactions would result in a highly interconnected pore network that enables the percolation of seawater through the serpentinite. The largest and most representative tomographic volumes presented in this study (Micro357 and Micro304) show the lowest (i.e., most interconnected) Euler characteristic values (Fig. 6). The reported connectivity values represent minima, because the voxel dimensions of our μ-CT data sets (1.6 μm) cannot capture the nanometer-scale pore structures detected with the FIB-SEM analyses (Fig. 2a, 2b, 4a, 4b). The latter are expected to act as pore throats that would further increase the interconnectivity of the pore structure. Whereas Euler characteristic values cannot be used to determine a quantitative threshold between open- and closed-system conditions, in samples Micro357 and Micro304 they define a highly interconnected network that, in concert with the previously outlined kinetic reasoning, suggests infiltration of weathering fluids that percolated through (and reacted with) the grain boundaries of olivine.

4.4. Elemental fluxes and implications

Low-temperature seafloor weathering processes result in elemental fluxes that increase seawater alkalinity and impose significant controls on the atmospheric concentration of CO_2 (Brady and Gíslason, 1997; Coogan and Gillis, 2018), exerting a negative feedback that removes carbon from the atmosphere at rates on par with continental weathering (Coogan and Gillis, 2013). Significant magnitudes of atmospheric CO_2 drawdown require comparable magnitudes of chemical fluxes between the oceanic crust and seawater. Snow and Dick (1995) initially suggested loss of Mg during low-temperature weathering of peridotite due to its interaction with seawater, which dramatically impacts the global Mg budget of the ocean. The removal of brucite from the mineralogic assemblage in altered peridotite (Beinlich et al., 2018) cannot explain the mass balance required to justify the degree of Mg loss (Snow and Dick, 1995; Klein et al., 2020) – i.e., olivine dissolution is required, and is exemplified by the textures reported in this study. Evidence of Mg exports comes from isotopic studies on altered oceanic crust (Huang et al., 2018), which revealed that the equivalent of ∼12% of the continental riverine input of Mg is extracted from the oceanic crust during low-temperature alteration. Several studies observed elemental mobility during alteration of peridotite both in experimental and natural seafloor settings (Snow and Dick, 1995; Lacinska et al., 2017). Moreover, recent studies on ophiolitic samples from Oman (de Obeso and Kelemen, 2020; de Obeso et al., 2021) reveal that Mg can be mobilized during alteration, as evidenced by the presence of meter-wide magnesite veins, and a loss of up to 30% of the original Mg content in the most altered rocks.

Dissolution of olivine during seafloor weathering of peridotite generates Si-enriched pore fluids that can contribute to the reservoir of biogenic silica used by silicifying organisms like radiolaria, sponges, and diatoms (Tréguer et al., 2021). Alternatively, dissolved Si and Mg can accumulate in pore fluids at stagnation points within the rock's pore network, becoming supersaturated with respect to secondary Mg-phyllosilicates that consequently precipitate from solution in a process known as reverse weathering (Tréguer et al., 2021). The absence of secondary Mg-phyllosilicates in our samples is likely attributable to the fine size of the observed pore structures, which is capable of suppressing the nucleation of secondary minerals (Putnis and Mauthe, 2001). In Table 2 we report an approximate estimation of the yearly flux of Mg removed from serpentinites due to dissolution of olivine based on the average pore volume quantified in samples Micro357 and Micro304. We obtain a yearly Mg flux of approximately 14.8 Gmol, which is one order of magnitude lower than the intermediate estimate calculated in Snow and Dick (1995), and corresponds to less than 1% of the yearly riverine input of Mg in seawater. Because samples Micro357 and Micro304 are relatively young (<2 m.y. old, Blackman et al., 2006), we can expect that export of Mg will continue in off-axis environments until (i) all remnants of olivine dissolve, or (ii) oceanic crustal rocks experience significant reduction in permeability that isolates them from seawater circulation, which is predicted to occur for crustal ages older than ∼65 m.y. (Coogan and Gillis, 2018). In fact, the tomographic data for Micro357 and Micro304 show the presence of remnants of olivine (Fig. 3), which occupy 7.01% and 4.13% of the tomographic volumes, respectively, and averaging at 5.57%. Following the calculation scheme summarized in Table 2, if we assume complete dissolution of the average volume of olivine remnants found in Micro357 and Micro304 and add this volume fraction (0.0557) to the weathered fraction based on the quantified pore volume (0.00445), we estimate a maximum yearly flux of 200 Gmol of Mg to seawater during low-temperature weathering of serpentinized peridotite.

5. Conclusions

In this study, we have reported the result of image processing of tomographic volumes acquired on serpentinized harzburgites recovered by drilling from the oceanic crust. Pore structures and their degree of connectivity have been characterized at the

Table 2
Estimation of the yearly Mg flux extracted during weathering of serpentinized peridotite according to the weathered fraction (Φ) quantified in this study.

Data		Results	
Ridge length (km)	14660[a]	Area created (m^2/yr)	167124
Exhumation rate (mm/yr)	11.4[a]	Weathered volume (m^3/yr)	2.84*10^8
Peridotite density (kg/m^3)	3300	Removed fraction (porosity) m^3	1.26*10^6
Molar mass Forsterite (kg/mol)	0.140691[b]	Dissolved mass (kg/yr)	4.17*10^9
Weathering depth (m)	1700[c]	Dissolved olivine (mol/yr)	2.97*10^10
Weathered fraction (Φ)	0.00445[d]	Mg flux (mol/yr)	1.48*10^10
Riverine Mg input (mol/yr)	5.5*10^12[e]	Fraction of riverine input (%)	0.27

[a] After Cannat et al. (2010). The ridge length is calculated as the proportion of global length of slow-spreading ridges that exhume new ultramafic crust. Due to the asymmetric exhumation that occurs along detachment faults at slow-spreading ridges, the exhumation rate is assumed to be equal to the average half-spreading rate at slow-spreading ridges.
[b] Molar mass calculated for pure forsterite endmember Mg_2SiO_4.
[c] Depth estimated by considering a maximum weathering temperature of 100 °C with a geothermal gradient of 60 °C/km.
[d] Calculated as the average total porosity quantified from tomographic data in samples Micro357 and Micro 304.
[e] After Elderfield and Schultz (1996); Berner and Berner (1987).

nanometer scale, at the scale of a single olivine crystal, and across the whole pore network at the micrometer scale. The presence of dissolution pores at the grain boundaries of olivine, the absence of secondary products in situ, and the preservation of serpentine minerals are consistent across all analyzed data sets. Our highest-resolution data sets revealed the presence of nanometric pores in the serpentine matrix, which we suggest formed due to serpentinization processes. We have also observed the presence of elongated dissolution channels, and recorded examples of lateral coalescence of these pore channels. The pores are preferentially oriented, likely due to a crystallographic preferred orientation inherited from olivine crystals. Observations on data sets Micro357 and Micro304 show that pores are found in clusters whose distribution in the rocks depends on the textural expression of olivine remnants (dissected olivine or isolated grains). When the dissolution pores are well developed, they form almost continuous envelopes around the remnants of olivine grains. Serpentinization is unlikely to have generated these observed pores, because they lack in situ secondary product that defines serpentinization. Rather, arguments based on kinetically controlled dissolution and precipitation rates indicate open-system conditions and rapid olivine dissolution rates, coupled to sluggish Mg-silicate and Mg-carbonate precipitation rates, which ultimately created the observed dissolution structures. In this way, the generation of pores during seafloor weathering of ultramafic rocks increases the permeability of the shallow oceanic lithosphere, maintains continued infiltration of seawater in the subsurface, and contributes to the global marine Si and Mg budgets.

CRediT authorship contribution statement

Simone Pujatti: Conceptualization, Formal analysis, Methodology, Writing – original draft. **Oliver Plümper:** Conceptualization, Methodology, Writing – review & editing. **Benjamin M. Tutolo:** Conceptualization, Methodology, Writing – review & editing.

Declaration of competing interest

The authors declare that they have no known competing financial interests or personal relationships that could have appeared to influence the work reported in this paper.

Data availability

Data will be made available on request.

Acknowledgements

This research used samples and data provided by the International Ocean Discovery Program (IODP). We acknowledge the support of the Natural Sciences and Engineering Research Council of Canada (NSERC) for providing funding for this research under Discovery Grant RGPIN-2018-03800. O. Plümper was supported by a European Research Council Starting grant (nanoEARTH; 852069). This study could not have been possible without the fellowship granted to S. Pujatti by Interridge in 2018. Part of the research described in this paper was performed at the Canadian Light Source, a national research facility of the University of Saskatchewan, which is supported by the Canada Foundation for Innovation (CFI), NSERC, the National Research Council (NRC), the Canadian Institutes of Health Research (CIHR), the Government of Saskatchewan, and the University of Saskatchewan. We would like to thank Dr. Sergey Gasilov for operating the high-energy Biomedical Imaging beamline of the Canadian Light Source (BMIT-ID) and for his help and commitment to providing high-quality tomographic reconstructions. Finally, we would like to thank two anonymous reviewers for their critical comments which helped to improve this paper's impact and clarity.

Appendix A. Supplementary material

Supplementary material related to this article can be found online at https://doi.org/10.1016/j.epsl.2023.118006.

References

Andréani, M., Baronnet, A., Boullier, A.M., Gratier, J.P., 2004. A microstructural study of a "crack-seal" type serpentine vein using SEM and TEM techniques. Eur. J. Mineral. 16 (4), 585–595. https://doi.org/10.1127/0935-1221/2004/0016-0585.

Andréani, M., Mével, C., Boullier, A.M., Escartin, J., 2007. Dynamic control on serpentine crystallization in veins: constraints on hydration processes in oceanic peridotites. Geochem. Geophys. Geosyst. 8 (2). https://doi.org/10.1029/2006gc001373.

Arizaleta, M.L., Nightingale, M., Tutolo, B.M., 2020. A rate law for sepiolite growth at ambient temperatures and its implications for early lacustrine diagenesis. Geochim. Cosmochim. Acta 288, 301–315. https://doi.org/10.1016/j.gca.2020.08.014.

Awad, A., Koster van Groos, A.F., Guggenheim, S., 2000. Forsteritic olivine: effect of crystallographic direction on dissolution kinetics. Geochim. Cosmochim. Acta 64 (10), 1765–1772. https://doi.org/10.1016/s0016-7037(99)00442-1.

Bach, W., Früh-Green, G.L., 2010. Alteration of the oceanic lithosphere and implications for seafloor processes. Elements 6 (3), 173–178. https://doi.org/10.2113/gselements.6.3.173.

Bach, W., Garrido, C.J., Paulick, H., Harvey, J., Rosner, M., 2004. Seawater-peridotite interactions: first insights from ODP Leg 209, MAR 15°N. Geochem. Geophys. Geosyst. 5 (9). https://doi.org/10.1029/2004gc000744.

Bach, W., Jöns, N., Klein, F., 2013. Metasomatism within the ocean crust. In: Metasomatism and the Chemical Transformation of Rock, pp. 253–288.

Bach, W., Rosner, M., Jöns, N., Rausch, S., Robinson, L.F., Paulick, H., Erzinger, J., 2011. Carbonate veins trace seawater circulation during exhumation and uplift of mantle rock: results from ODP Leg 209. Earth Planet. Sci. Lett. 311 (3–4), 242–252. https://doi.org/10.1016/j.epsl.2011.09.021.

Bales, R.C., Morgan, J.J., 1985. Dissolution kinetics of chrysotile at pH 7 to 10. Geochim. Cosmochim. Acta 49 (11), 2281–2288. https://doi.org/10.1016/0016-7037(85)90228-5.

Beinlich, A., Austrheim, H., Mavromatis, V., Grguric, B., Putnis, C.V., Putnis, A., 2018. Peridotite weathering is the missing ingredient of Earth's continental crust composition. Nat. Commun. 9 (1). https://doi.org/10.1038/s41467-018-03039-9.

Berner, E.K., Berner, R.A., 1987. Global Water Cycle: Geochemistry and Environment. Prentice-Hall, Inc., Englewood Cliffs New Jersey, p. 397.

Berninger, U.-N., Jordan, G., Schott, J., Oelkers, E.H., 2014. The experimental determination of hydromagnesite precipitation rates at 22.5–75 °C. Mineral. Mag. 78 (6), 1405–1416. https://doi.org/10.1180/minmag.2014.078.6.07.

Blackman, D.K., Ildefonse, B., John, B.E., Ohara, Y., Miller, D.J., Macleod, C.J., 2006. Expedition 304/305 scientists (2006). Expedition 304/305 summary. In: Proceedings of the Integrated Ocean Drilling Program, vol. 304, p. 305.

Boudier, F., Baronnet, A., Mainprice, D., 2010. Serpentine mineral replacements of natural olivine and their seismic implications: oceanic lizardite versus subduction-related antigorite. J. Petrol. 51 (1–2), 495–512. https://doi.org/10.1093/petrology/egp049.

Brady, P.V., Gíslason, S.R., 1997. Seafloor weathering controls on atmospheric CO2 and global climate. Geochim. Cosmochim. Acta 61 (5), 965–973. https://doi.org/10.1016/s0016-7037(96)00385-7.

Cannat, M., Fontaine, F., Escartín, J., 2010. Serpentinization and associated hydrogen and methane fluxes at slow spreading ridges. In: Diversity of Hydrothermal Systems on Slow Spreading Ocean Ridges, pp. 241–264.

Che, Z., Nightingale, M., Tutolo, B.M., 2021. Probing the application of kinetic theory to Mg-phyllosilicate growth with Si isotope doping. Geochim. Cosmochim. Acta 310, 205–220. https://doi.org/10.1016/j.gca.2021.05.025.

Coogan, L.A., Gillis, K.M., 2013. Evidence that low-temperature oceanic hydrothermal systems play an important role in the silicate-carbonate weathering cycle and long-term climate regulation. Geochem. Geophys. Geosyst. 14 (6), 1771–1786. https://doi.org/10.1002/ggge.20113.

Coogan, L.A., Gillis, K.M., 2018. Low-temperature alteration of the seafloor: impacts on ocean chemistry. Annu. Rev. Earth Planet. Sci. 46 (1), 21–45. https://doi.org/10.1146/annurev-earth-082517-010027.

Cooperdock, E.H.G., Stockli, D.F., 2018. Dating exhumed peridotite with spinel (U–Th)/He chronometry. Earth Planet. Sci. Lett. 489, 219–227. https://doi.org/10.1016/j.epsl.2018.02.041.

de Obeso, J.C., Kelemen, P.B., 2020. Major element mobility during serpentinization, oxidation and weathering of mantle peridotite at low temperatures. Philos. Trans. R. Soc. A, Math. Phys. Eng. Sci. 378 (2165), 20180433. https://doi.org/10.1098/rsta.2018.0433.

de Obeso, J.C., Santiago Ramos, D.P., Higgins, J.A., Kelemen, P.B., 2021. A Mg isotopic perspective on the mobility of magnesium during serpentinization and carbonation of the Oman ophiolite. J. Geophys. Res., Solid Earth 126 (2). https://doi.org/10.1029/2020jb020237.

Elderfield, H., Schultz, A., 1996. Mid-ocean ridge hydrothermal fluxes and the chemical composition of the ocean. Annu. Rev. Earth Planet. Sci. 24 (1), 191–224. https://doi.org/10.1146/annurev.earth.24.1.191.

Faragó, T., Gasilov, S., Emslie, I., Zuber, M., Helfen, L., Vogelgesang, M., Baumbach, T., 2022. Tofu: a fast, versatile and user-friendly image processing toolkit for computed tomography. J. Synchrotron Radiat. 29 (3), 916–927. https://doi.org/10.1107/s160057752200282x.

Früh-Green, G.L., Orcutt, B.N., Green, S.L., Cotterill, C., the Expedition 357 Scientists, 2017. Atlantis Massif serpentinization and life. In: Proceedings of the International Ocean Discovery Program, 357. International Ocean Discovery Program, College Station, TX. https://doi.org/10.14379/iodp.proc.357.2017.

Fuhr, M., Geilert, S., Schmidt, M., Liebetrau, V., Vogt, C., Ledwig, B., Wallmann, K., 2022. Kinetics of olivine weathering in seawater: an experimental study. Front. Clim. 39. https://doi.org/10.3389/fclim.2022.831587.

Grandstaff, D.E., 1978. Changes in surface area and morphology and the mechanism of forsterite dissolution. Geochim. Cosmochim. Acta 42 (12), 1899–1901. https://doi.org/10.1016/0016-7037(78)90245-4.

Grimes, C.B., John, B.E., Cheadle, M.J., Wooden, J.L., 2008. Protracted construction of gabbroic crust at a slow spreading ridge: constraints from 206Pb/238U zircon ages from Atlantis Massif and IODP Hole U1309D (30°N, MAR). Geochem. Geophys. Geosyst. 9 (8). https://doi.org/10.1029/2008gc002063.

Huang, K.-J., Teng, F.-Z., Plank, T., Staudigel, H., Hu, Y., Bao, Z.-Y., 2018. Magnesium isotopic composition of altered oceanic crust and the global Mg cycle. Geochim. Cosmochim. Acta 238, 357–373. https://doi.org/10.1016/j.gca.2018.07.011.

Jöns, N., Kahl, W.-A., Bach, W., 2017. Reaction-induced porosity and onset of low-temperature carbonation in abyssal peridotites: insights from 3D high-resolution microtomography. Lithos 268–271, 274–284. https://doi.org/10.1016/j.lithos.2016.11.014.

Kelemen, P.B., Hirth, G., 2012. Reaction-driven cracking during retrograde metamorphism: olivine hydration and carbonation. Earth Planet. Sci. Lett. 345–348, 81–89. https://doi.org/10.1016/j.epsl.2012.06.018.

Kelemen, P.B., Matter, J., Streit, E.E., Rudge, J.F., Curry, W.B., Blusztajn, J., 2011. Rates and mechanisms of mineral carbonation in peridotite: natural processes and recipes for enhanced, in situ CO2 capture and storage. Annu. Rev. Earth Planet. Sci. 39 (1), 545–576. https://doi.org/10.1146/annurev-earth-092010-152509.

Kelemen, P.B., Kikawa, E., Miller, D.J., et al., 2004. In: Proc. ODP, Init. Repts., vol. 209. Ocean Drilling Program, College Station, TX.

King, H.E., Satoh, H., Tsukamoto, K., Putnis, A., 2014. Surface-specific measurements of olivine dissolution by phase-shift interferometry. Am. Mineral. 99 (2–3), 377–386. https://doi.org/10.2138/am.2014.4606.

Klein, F., Humphris, S.E., Bach, W., 2020. Brucite formation and dissolution in oceanic serpentinite. Geochem. Perspect. Lett. 16, 1–5. https://doi.org/10.7185/geochemlet.2035.

Krissansen-Totton, J., Catling, D.C., 2017. Constraining climate sensitivity and continental versus seafloor weathering using an inverse geological carbon cycle model. Nat. Commun. 8 (1), 1–15. https://doi.org/10.1038/ncomms15423.

Lacinska, A.M., Styles, M.T., Bateman, K., Hall, M., Brown, P.D., 2017. An experimental study of the carbonation of serpentinite and partially serpentinised peridotites. Front. Earth Sci. 5, 37. https://doi.org/10.3389/feart.2017.00037.

Lafay, R., Montes-Hernandez, G., Janots, E., Chiriac, R., Findling, N., Toche, F., 2012. Mineral replacement rate of olivine by chrysotile and brucite under high alkaline conditions. J. Cryst. Growth 347 (1), 62–72. https://doi.org/10.1016/j.jcrysgro.2012.02.040.

Luce, R.W., Bartlett, R.W., Parks, G.A., 1972. Dissolution kinetics of magnesium silicates. Geochim. Cosmochim. Acta 36 (1), 35–50. https://doi.org/10.1016/0016-7037(72)90119-6.

Mulders, J.J.P.A., Oelkers, E.H., 2021. An experimental study of sepiolite dissolution and growth rates as function of the aqueous solution saturation state at 60 °C. Geochim. Cosmochim. Acta 315, 276–294. https://doi.org/10.1016/j.gca.2021.09.004.

Oelkers, E.H., Declercq, J., Saldi, G.D., Gislason, S.R., Schott, J., 2018. Olivine dissolution rates: a critical review. Chem. Geol. 500, 1–19. https://doi.org/10.1016/j.chemgeo.2018.10.008.

Osselin, F., Pichavant, M., Champallier, R., Ulrich, M., Raimbourg, H., 2022. Reactive transport experiments of coupled carbonation and serpentinization in a natural serpentinite. Implication for hydrogen production and carbon geological storage. Geochim. Cosmochim. Acta 318, 165–189. https://doi.org/10.1016/j.gca.2021.11.039.

Paganin, D., Mayo, S.C., Gureyev, T.E., Miller, P.R., Wilkins, S.W., 2002. Simultaneous phase and amplitude extraction from a single defocused image of a homogeneous object. J. Microsc. 206 (1), 33–40. https://doi.org/10.1046/j.1365-2818.2002.01010.x.

Peuble, S., Andréani, M., Godard, M., Gouze, P., Barou, F., Van de Moortele, B., et al., 2015. Carbonate mineralization in percolated olivine aggregates: linking effects of crystallographic orientation and fluid flow. Am. Mineral. 100 (2–3), 474–482. https://doi.org/10.2138/am-2015-4913.

Plümper, O., Røyne, A., Magrasó, A., Jamtveit, B., 2012. The interface-scale mechanism of reaction-induced fracturing during serpentinization. Geology 40 (12), 1103–1106. https://doi.org/10.1130/g33390.1.

Power, I.M., Kenward, P.A., Dipple, G.M., Raudsepp, M., 2017. Room temperature magnesite precipitation. Cryst. Growth Des. 17 (11), 5652–5659. https://doi.org/10.1021/acs.cgd.7b00311.

Putnis, A., Mauthe, G., 2001. The effect of pore size on cementation in porous rocks. Geofluids 1 (1), 37–41. https://doi.org/10.1046/j.1468-8123.2001.11001.x.

Seyfried Jr., W.E., Pester, N.J., Tutolo, B.M., Ding, K., 2015. The Lost City hydrothermal system: constraints imposed by vent fluid chemistry and reaction path models on subseafloor heat and mass transfer processes. Geochim. Cosmochim. Acta 163, 59–79. https://doi.org/10.1016/j.gca.2015.04.040.

Snow, J.E., Dick, H.J.B., 1995. Pervasive magnesium loss by marine weathering of peridotite. Geochim. Cosmochim. Acta 59 (20), 4219–4235. https://doi.org/10.1016/0016-7037(95)00239-v.

Tosca, N.J., 2015. Geochemical pathways to Mg-clay formation. In: Magnesian Clays: Characterization, Origin and Applications. In: AIPEA Special Publication, vol. 2, pp. 283–329.

Tréguer, P.J., Sutton, J.N., Brzezinski, M., Charette, M.A., Devries, T., Dutkiewicz, S., Ehlert, C., Hawkings, J., Leynaert, A., Liu, S.M., Llopis Monferrer, N., López-Acosta, M., Maldonado, M., Rahman, S., Ran, L., Rouxel, O., 2021. Reviews and syntheses: the biogeochemical cycle of silicon in the modern ocean. Biogeosciences 18 (4), 1269–1289. https://doi.org/10.5194/bg-18-1269-2021.

Tutolo, B.M., Luhmann, A.J., Tosca, N.J., Seyfried, W.E., 2018. Serpentinization as a reactive transport process: the brucite silicification reaction. Earth Planet. Sci. Lett. 484, 385–395. https://doi.org/10.1016/j.epsl.2017.12.029.

Tutolo, B.M., Mildner, D.F.R., Gagnon, C.V.L., Saar, M.O., Seyfried, W.E., 2016. Nanoscale constraints on porosity generation and fluid flow during serpentinization. Geology 44 (2), 103–106. https://doi.org/10.1130/g37349.1.

Velbel, M.A., 2009. Dissolution of olivine during natural weathering. Geochim. Cosmochim. Acta 73 (20), 6098–6113. https://doi.org/10.1016/j.gca.2009.07.024.

Vogel, H.-J., Weller, U., Schlüter, S., 2010. Quantification of soil structure based on Minkowski functions. Comput. Geosci. 36 (10), 1236–1245. https://doi.org/10.1016/j.cageo.2010.03.007.

Warren, J.M., 2016. Global variations in abyssal peridotite compositions. Lithos 248–251, 193–219. https://doi.org/10.1016/j.lithos.2015.12.023.

Wysokinski, T.W., Chapman, D., Adams, G., Renier, M., Suortti, P., Thomlinson, W., 2015. Beamlines of the biomedical imaging and therapy facility at the Canadian light source – part 3. Nucl. Instrum. Methods Phys. Res., Sect. A, Accel. Spectrom. Detect. Assoc. Equip. 775, 1–4. https://doi.org/10.1016/j.nima.2014.11.088.

Xiong, W., Giammar, D., 2014. Forsterite carbonation in zones with transport limited by diffusion. Environ. Sci. Technol. Lett. 1 (8), 333–338. https://doi.org/10.1021/ez500182s.

Yu, Y., Tikoff, B., 2020. Magnetic Cr-rich spinel in serpentinized ultramafic complexes. J. Geophys. Res., Solid Earth 125 (11). https://doi.org/10.1029/2020jb020443.